Radio-Frequency Interference Mitigation for the Soil Moisture Active Passive Microwave Radiometer

Jeffrey R. Piepmeier, *Senior Member, IEEE*, Joel T. Johnson, *Fellow, IEEE*, Priscilla N. Mohammed, *Member, IEEE*, Damon Bradley, *Member, IEEE*, Christopher Ruf, *Fellow, IEEE*, Mustafa Aksoy, Rafael Garcia, Derek Hudson, Lynn Miles, and Mark Wong

***Abstract*—The Soil Moisture Active Passive (SMAP) radiometer operates in the L-band protected spectrum (1400–1427 MHz) that is known to be vulnerable to radio-frequency interference (RFI). Although transmissions are forbidden at these frequencies by international regulations, ground-based, airborne, and spaceborne radiometric observations show substantial evidence of out-of-band emissions from neighboring transmitters and possibly illegally operating emitters. The spectral environment that SMAP faces includes not only occasional large levels of RFI but also significant amounts of low-level RFI equivalent to a brightness temperature of 0.1–10 K at the radiometer output. This low-level interference would be enough to jeopardize the success of a mission without an aggressive mitigation solution, including special flight hardware and ground software with capabilities of RFI detection and removal. SMAP takes a multidomain approach to RFI mitigation by utilizing an innovative onboard digital detector back end with digital signal processing algorithms to characterize the time, frequency, polarization, and statistical properties of the received signals. Almost 1000 times more measurements than what is conventionally necessary are collected to enable the ground processing algorithm to detect and remove harmful interference. Multiple RFI detectors are run on the ground, and their outputs are combined for maximum likelihood of detection to remove the RFI within a footprint. The capabilities of the hardware and software systems are successfully demonstrated using test data collected with a SMAP radiometer engineering test unit.**

***Index Terms*—Microwave radiometry, radio frequency interference.**

Manuscript received September 11, 2012; revised February 4, 2013 and June 3, 2013; accepted June 5, 2013.

J. R. Piepmeier is with the Microwave Instrument Technology Branch, NASA's Goddard Space Flight Center, Greenbelt, MD 20771 USA.

J. T. Johnson is with The ElectroScience Laboratory and the Department of Electrical and Computer Engineering, College of Engineering, The Ohio State University, Columbus, OH 43210 USA.

P. N. Mohammed is with Goddard Earth Sciences Technology and Research (GESTAR), Universities Space Research Association, Columbia, MD 21044 USA, and also with the Microwave Instrument Technology Branch, NASA's Goddard Space Flight Center, Greenbelt, MD 20771 USA.

D. Bradley is with the University of Maryland, Baltimore, MD 21250 USA, and also with the Digital Signal Processing Technology Group, Instrument Electronics Development Branch, NASA's Goddard Space Flight Center, Greenbelt, MD 20771 USA.

C. Ruf is with the Space Physics Research Laboratory, College of Engineering, University of Michigan, Ann Arbor, MI 48109-2143 USA.

M. Aksoy is with The ElectroScience Laboratory, College of Engineering, The Ohio State University, Columbus, OH 43210 USA.

R. Garcia, D. Hudson, and M. Wong are with NASA's Goddard Space Flight Center, Greenbelt, MD 20771 USA.

L. Miles is with the Digital Signal Processing Technology Group, Instrument Electronics Development Branch, NASA's Goddard Space Flight Center, Greenbelt, MD 20771 USA.

Color versions of one or more of the figures in this paper are available online at http://ieeexplore.ieee.org.

Digital Object Identifier 10.1109/TGRS.2013.2281266

I. Introduction and Background

THE Soil Moisture Active Passive (SMAP) mission is expected to provide global high-resolution active–passive L-band observations of the Earth from space [1]. The microwave radiometer's prime science objective is to provide soil-moisture measurements with an uncertainty of < 0.04 $\mathrm{m^3 m^{-3}}$ for terrain having vegetation water contents of up to 5 $\mathrm{kg/m^2}$, which requires a radiometric uncertainty of $<$ 1.3 K [1]. The consequences of allowing RFI to corrupt the radiometer measurements are either nonphysical (negative valued) soil moisture, or sporadic or persistent dry biases. The latter result is quite insidious because undetected RFI could be mistaken for environmental signatures. Thus, there exists a compelling justification for aggressively mitigating RFI in SMAP.

The problem of RFI in spaceborne microwave radiometer measurements has been known for at least three decades. As early as 1978, RFI has been observed at the C-band in data from the Scanning Multichannel Microwave Radiometer, which was used for measuring sea surface temperature [2]. More recently, interference at C-, X-, and K-bands has been apparent in data from AMSR-E and WindSat [3]–[5]. As the observation frequency decreased, from centimeter to decimeter wavelengths (i.e., L-band at 1.4 GHz), the problem has become more pronounced. Indeed, significant RFI contamination of radiometric measurements from ESA's Soil Moisture and Ocean Salinity (SMOS) mission is evident [6]. Although radio spectrum managers work within the radio regulations to enable compatibility between active and passive RF systems, there is no guarantee (even if all the rules are followed) that radiometer observations will be RFI free [7]. Fortunately, solutions to mitigate the deleterious effects of interference have been demonstrated in recent systems. The Aquarius radiometers on SAC-D and their ground processing software comprise the first of such spaceborne systems that are designed to detect and remove much of the interference caused by ground-based radar systems [8]–[11]. Fortunately, the last decade has seen a concerted effort to develop and mature more advanced RFI mitigation technology to be used in spaceborne radiometers [12], [13]. Leveraging these technologies, the comprehensive approach for RFI mitigation taken by the SMAP team is described herein.

The SMAP RFI mitigation system utilizes a combination of space-flight instrument hardware and ground-based science processing algorithms. First, efforts to characterize the RFI environment and to test various RFI detection techniques from aircraft are reviewed in Section II. The result of these efforts was a decision to employ an advanced digital microwave radiometer,

which is the first of its kind for space flight, for use on SMAP. Whereas conventional radiometers output detector counts that are proportional to the receiver-system noise temperature, the SMAP radiometer outputs the first four raw moments of the receiver-system noise voltage in 16 frequency channels for measuring noise temperature and kurtosis, as well as complex cross-correlation products for measuring the third and fourth Stokes parameters. The features and operation of the radiometer are presented in Section III, and the associated ground-based science processing algorithms are discussed in Section IV. The algorithm utilizes several detectors to identify RFI in the frequency, time, statistical, and polarization domains measured by the instrument. The outputs of the detectors are combined to maximize the probability of detection (PD) and to remove the contaminated time–bandwidth portions of the observation. The performance of these algorithms is demonstrated in Section V using data from the radiometer engineering test unit (ETU).

II. Characterization of the RFI Environment

Characterization of the RFI environment for the SMAP radiometer [14]–[16] is conducted through a multifaceted approach that includes predictions based on known properties of existing sources [9], examination of observations from ground-based [17], [18] or aircraft-based [19]–[21] radiometers, and analysis of satellite data sets from SMOS [22]–[29] and Aquarius [8], [10], [11].

A. Predictions Based on Properties of Known Sources

Because SMAP operates nominally in the protected allocated 1400–1427 MHz of the Earth Exploration Satellite Service, no sources are licensed nor permitted to operate within the SMAP band, and information on sources operating illegally within the SMAP band is not readily available. Nevertheless, sources operating legally outside the SMAP band can cause RFI to SMAP using two mechanisms. In the first mechanism, the SMAP frequency response may be insufficient to eliminate the influence of radiation transmitted at frequencies outside the range of 1400–1427 MHz. Because the SMAP filters are designed to have high rejection outside this range, this is primarily a concern for sources operating very near the 1400–1427 region (e.g., in the range of 1395–1400 MHz). The second mechanism occurs when sources that are nominally operating outside the SMAP band produce small levels of emissions in the range of 1400–1427 MHz [30]. These emissions are allowed by regulations but are required to be well below the transmitted power of the source. This second out-of-band (OOB) mechanism for coupling to SMAP is a key concern, particularly due to the very high power transmissions of many operating L-band radar systems.

An analysis of the potential OOB effects on SMAP was conducted through simulations of SMAP observations of known radar facilities in North America [9]. Simulations of SMAP observations of radar transmissions (based on known source transmit properties and standard properties of the OOB emission mask of these sources) were performed, and statistics of RFI power levels were compiled. These simulations showed that very high received power levels of up to 2 W were possible in some situations; the maximum power levels were used to determine survivability power levels for the SMAP radiometer electronics. In addition, the simulations showed that RFI corruption could occur with frequencies and power levels that are sufficient to affect SMAP science products. Because radar transmissions are pulsed, a pulse detection method used to oversample the radiometer measurements in time (as conducted for Aquarius [10], [11]) was originally proposed (for the SMAP precursor HYDROS mission [46]) as sufficient to mitigate these concerns [9].

The analyses conducted were limited by the fact that only radar sources in North America were considered. Although these studies are expected to be reliable for survivability and regional concerns, the inclusion of global information for a variety of source types is clearly required to improve the understanding of the SMAP RFI environment.

B. Ground- and Aircraft-Based Observations

Early augmentation of the results from the RFI prediction studies involved incorporating information from ground-based observations [17], [18]. Although this information is limited in space and time, it includes measured characteristics of the observed sources, regardless of their legality, and can provide detailed information (e.g., frequencies, power levels, bandwidths, and even modulation types in some situations) that is valuable in describing the RFI environment. Obtaining detailed source characterization information requires measurement equipment with these capabilities; it is desirable if this equipment is also capable of operating as a radiometer to assess radiometric performance in the presence of interference. Accordingly, radiometer systems with advanced digital back ends for RFI detection and mitigation [19] were included in SMAP RFI studies. The results of these analyses showed the clear presence of spurious emissions (or perhaps sources operating illegally) in the protected band and provided information on the wideband pulsed nature of OOB emissions of L-band radar systems. The sources observed within the protected band from the ground-based locations considered were primarily of the narrow-band type, which are mostly spurious emissions from nearby communication systems occupying bandwidths of 1 MHz or less. These source types would be difficult to detect and mitigate with a pulse detection strategy alone.

Aircraft-based observations [19]–[21] provide an opportunity to expand the spatial coverage of RFI environment characterization beyond that available from ground-based studies. Existing airborne data sets acquired for the SMOS mission were examined [20], [21] and augmented by a dedicated set of RFI observations for SMAP [19] that were performed as part of the SMAP Validation Experiment in 2008 (SMAPVEX08). Fig. 1 (see [19]) illustrates the locations of the nine aircraft flights (approximately a total of 24 flight hours) used for RFI studies; two digital and one analog back-end systems were included for RFI detection and mitigation analysis. The results again showed the presence of both OOB emissions (and possibly illegal sources) inside the protected band. A variety of source

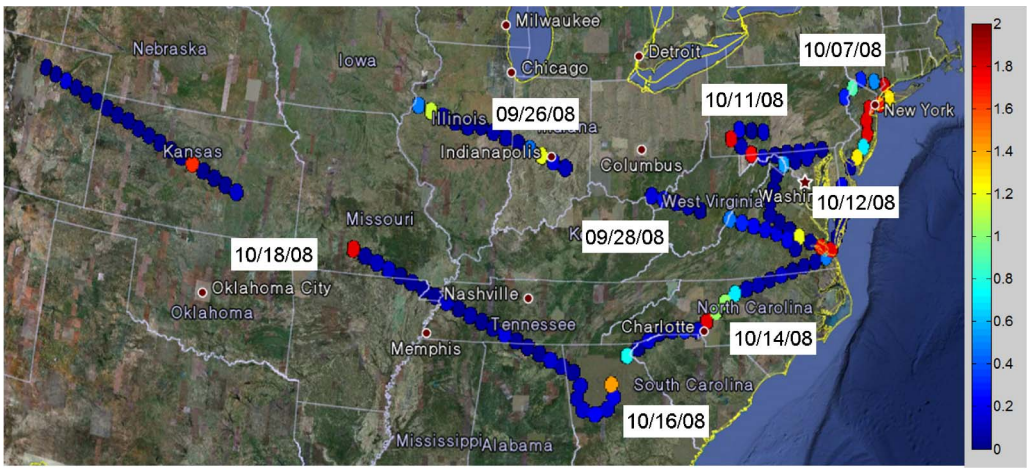

Fig. 1. SMAPVEX08 flight paths utilized in RFI analysis (excluding 10/6/08 data). Geolocated RFI brightness temperatures at a spatial resolution of 40 km and with H polarization (colorscale in kelvin). From [19] with permission from the author.

characteristics, including pulsed, narrow-band [i.e., near continuous wave (CW)], and wideband types, was observed.

A scaling procedure, which is described in [19] and essentially involves spatial averaging of the aircraft data, was used to forecast statistics of expected RFI levels for the SMAP radiometer. Because the resulting RFI levels would significantly impact SMAP science products and the existing RFI detection and mitigation approach based on oversampling in time would be ineffective for many of the sources observed, the SMAP project in early 2009 modified the radiometer design to include a digital back end to improve RFI detection and mitigation performance.

C. Satellite Observations

Expansion of RFI environment characterization to include global information is possible only through the inclusion of global satellite measurements. The availability of L-band radiometer measurements from ESA's SMOS mission (beginning November 2009) and from NASA's Aquarius/SAC-D mission (beginning August 2011) allows global information to be obtained. Both missions have clearly shown the presence of RFI corruption. Fig. 2 for example shows the maximum values of Aquarius horizontally polarized measurements from April 28, 2012 to May 26, 2012 (using all Aquarius radiometer beams) on a $0.5^\circ \times 0.5^\circ$ gridded Earth model. Large RFI sources are observed on every continent; it is noted that North America shows reduced corruption compared with Europe and Asia, underscoring the importance of global information, as compared with that previously focused on North America alone.

The compilation of SMOS and Aquarius brightness-temperature statistics over land regions within the expected SMAP soil-moisture retrieval area is straightforward. SMOS data (which include observations over a range of incidence angles) are selected within 2.5° of SMAP's nominal 40° incidence angle, and the middle Aquarius beam (37.8° incidence angle) is considered. Although a variety of RFI detection and mitigation approaches has been considered for SMOS [24]–[29], reported SMOS products to date do not include an estimate of RFI levels; therefore, only the SMOS brightness temperature itself is

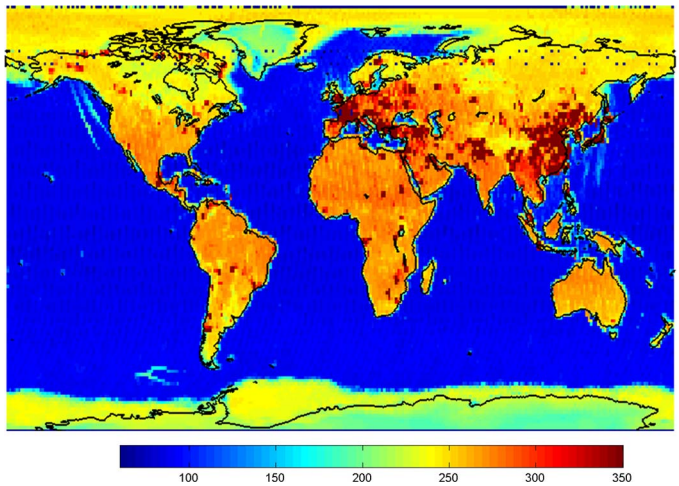

Fig. 2. Maximum Aquarius L-band horizontally polarized brightness temperature encountered on a 0.5° latitude by 0.5° longitude global grid over the period of April 28, 2012 to May 26, 2012. All Aquarius antenna beams are included.

examined. In general, the detection of low-level RFI in SMOS is difficult; therefore, information sought from SMOS will focus on the presence of large sources that are clearly distinguishable from geophysical effects. It is also noted that RFI corruption of SMOS observations is caused not only by RFI sources within the radiometer main beams but also by artifacts associated with imaging aliases or sidelobes [27], [30]. Therefore, RFI source occurrence probabilities obtained from SMOS measurements are likely to be overestimates of the presence of "true" sources.

In contrast to SMOS, the Aquarius radiometer ground processor includes a pulse detection algorithm (based on its oversampling of the radiometer measurements in time), allowing RFI contributions (including low-level contributions) to be estimated. While this algorithm is well suited to detect pulsed interference from radar transmissions, it is largely inapplicable to low-to-moderate-level CW-type sources. Therefore, RFI information obtained from Aquarius should be expected in some aspects to be a lower bound on "true" source properties. As in

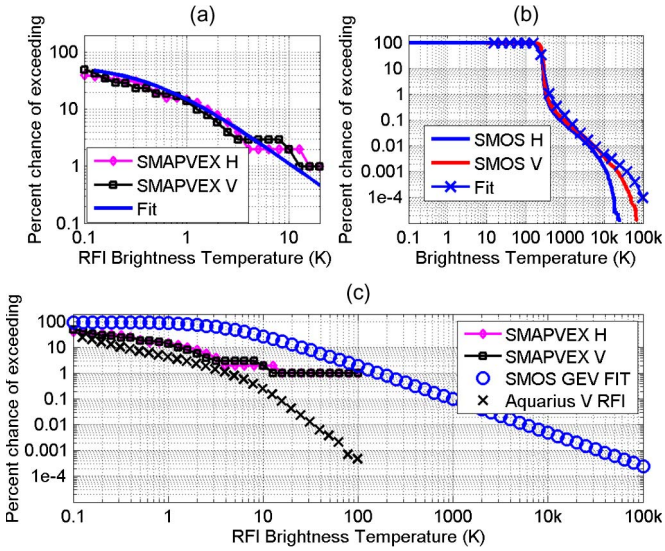

Fig. 3. (Upper left) CCDFs of observed RFI levels from the SMAPVEX08 airborne campaign, and the associated fit with GEV distribution. (upper right) CCDFs of SMOS horizontally and vertically polarized brightness temperatures for the period of November 15, 2011 to December 15, 2011. The fit to these curves as sum of Gaussian (for geophysical contributions) and GEV (for RFI) random variables are also illustrated. (Bottom) GEV fit of SMOS RFI only ccdf compared with SMAPVEX08 and Aquarius RFI-only ccdfs.

SMOS, RFI contributions from sources in the sidelobes of the Aquarius antenna are also observed.

Additional methods to apply RFI information derived from SMOS and Aquarius to SMAP are discussed in [31]; these methods involve "scaling approaches" that are largely based on consideration of the differences in spatial resolutions and temporal sampling between the missions. Because SMOS and SMAP have similar spatial resolution and coverage, scaling has only a modest impact and is not applied to the SMOS statistics shown in the following. The larger Aquarius spatial resolution of 84 km by 120 km in the middle beam results in a footprint area that is 6.3 times larger than SMAP. Therefore, the RFI power levels observed by Aquarius could be increased by a factor of 6.3 to represent SMAP observations of RFI within its main beam. However, scaling the frequency of occurrence of RFI requires more detailed consideration [31]. For simplicity, Aquarius measurements are not scaled in the following, although the potential impact of scaling will be discussed when appropriate.

D. Current RFI Environment Characterization

The upper left plot in Fig. 3 shows the complementary cumulative distribution functions (ccdfs) of the detected RFI levels obtained from the SMAPVEX08 aircraft observations in horizontal and vertical polarizations (H and V polarizations) after scaling to represent SMAP measurements. These low-level contributions show a near linear behavior on the log–log axes utilized, suggesting that the dependence values could be reasonably approximated using a power-law analytical form. By taking the RFI level in one of the SMAPVEX08 observations as a random variable, it was found that a generalized extreme value (GEV) distribution [32] could provide a reasonable fit to the SMAPVEX08 RFI levels, as shown in the upper left plot in Fig. 3. A GEV random variable has a ccdf of

$$F(T) = 1 - \exp\left\{-\left[1 + a\left(\frac{T-\mu}{\sigma}\right)\right]^{-\frac{1}{a}}\right\} \approx \left(\frac{\sigma}{aT}\right)^{a} \quad (1)$$

where T is the RFI brightness temperature (in kelvin), and σ, μ, and a are the parameters of the ccdf. The large T limit shown in the second line of (1) clarifies that a and σ are determined by the slope and the amplitude, respectively, of the measured ccdf at large values. The remaining μ parameter is an offset; if μ is chosen to be greater than σ/a, the probability of obtaining negative values is zero.

The red and blue curves in the upper right plot in Fig. 3 illustrate the ccdfs of SMOS horizontally and vertically polarized brightness temperatures ($40+/-2.5^{\circ}$) over the SMAP land soil-moisture retrieval area for the period of November 15, 2011 to December 15, 2011. Unlike the SMAPVEX08 results, these data include both geophysical and RFI contributions. The results show typically expected geophysical behaviors (i.e., nearly 100% of the observations have brightness temperatures that are approximately greater than 200 K, followed by a rapid decrease in brightness temperatures approximately greater than 300 K) but also include long tails that are indicative of RFI. The tails are similar for H and V polarizations but are somewhat larger in the V polarization. As mentioned previously, it is not currently possible to derive information on low-to-moderate-level RFI (i.e., having brightness-temperature contributions of < 100 K) directly from SMOS measurements.

The reasonable success of the GEV form in matching the SMAPVEX08 RFI data suggests an approach for attempting to separate RFI from geophysical contributions in the SMOS ccdf. The procedure assumes that SMOS individual observations can be represented as a sum of a GEV random variable (for RFI) and an independent Gaussian random variable (for geophysical contributions). The latter is a significant assumption since global brightness temperatures do not necessarily follow a Gaussian form. By accepting this assumption at least initially, the simulated ccdfs for the combined observation can be then produced as a function of the GEV random variable parameters and the two parameters (mean and standard deviation) of the geophysical random variable. The parameters can then be varied to seek a match to the observed SMOS ccdf. Note that only the μ parameter of the GEV portion is allowed to vary since a and σ are determined without tuning using the ccdf at large brightness temperatures. The curve labeled "fit" in the upper right plot in Fig. 3 was obtained through this process, and is a reasonable match to the measured SMOS ccdfs.

Given a reasonable fit to the total brightness-temperature ccdf, the ccdf of the GEV portion alone (which represents RFI brightness temperatures) can be used as a prediction of low-to-moderate-level RFI derived from SMOS observations. The "SMOS GEV fit" curve in the lower plot in Fig. 3 is the estimated RFI ccdf obtained from this procedure with vertically polarized brightness temperatures, with the parameters determined as $a = 0.77$, $\sigma = 3.75$ K, and $\mu = 3.2$ K. Note that

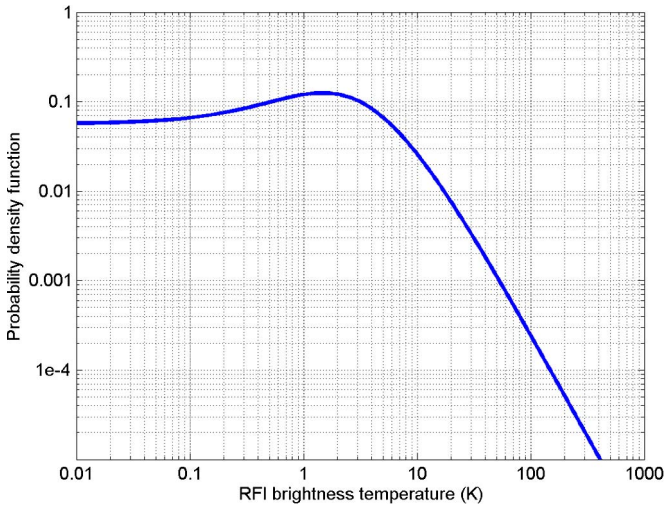

Fig. 4. RFI brightness-temperature pdf derived from SMOS GEV extrapolation.

these parameters do not satisfy $\mu > \sigma/a$; therefore, a small percentage of negative RFI values are predicted, indicating the limitations of the procedure. Other combinations of parameters are also possible to produce similar fitting performance, but the given parameters were deemed reasonable based on the overall agreement achieved and the examination of SMOS data over multiple time periods. The resulting SMOS RFI extrapolation produces low-level RFI predictions that are significantly higher than those obtained from SMAPVEX08. However, such behavior is expected due to the increased RFI encountered outside North America.

Further RFI environment information is included in the lower plot in Fig. 3 by including a ccdf of the Aquarius-detected RFI in V polarization. A first examination shows that large RFI brightness temperatures occur much less frequently in the Aquarius data set as compared with the SMOS data set. However, this conclusion is influenced by the fact that the Aquarius radiometer, in some cases, reports observations with significant RFI corruption as invalid; therefore, the Aquarius-detected RFI level cannot be determined (and is therefore excluded from the data set plotted). In addition, applying a scaling process will increase Aquarius RFI brightness temperatures by a factor of 6.3 while shifting the frequency of occurrence by an additional factor. The limitations of Aquarius with respect to detecting continuous source types also suggest that RFI "truth" would be larger than the Aquarius observations.

Due to the clear uncertainties that remain in producing a robust prediction of the SMAP RFI environment, as well as the potential evolution of the RFI environment in time, the SMAP mission is currently adopting a conservative approach by utilizing the SMOS GEV extrapolation to characterize RFI statistics over the SMAP soil-moisture retrieval area. This approach, for example, specifies that 10% of SMAP observations will contain RFI of 20 K or more. The corresponding RFI brightness-temperature probability density function (pdf), shown in Fig. 4, contains a significant presence of low-level RFI with a brightness temperature of 1 K or less, and represents a challenging environment for RFI performance tests. Simulations of SMAP radiometer RFI detection and mitigation performance in this environment will be further discussed in Section V. Current results of such simulations show success in meeting science requirements for this environment (given a wide range of RFI source types) and indicate a high likelihood of meeting science requirements once on orbit.

III. SMAP Radiometer Hardware Design

A significant aspect of the SMAP radiometer design is the utilization of an advanced digital signal processing (DSP) back end. Rather than using square-law diode detectors and analog integrators found on conventional spaceborne microwave radiometers, the radiometer digital electronics (RDE) samples receiver signals and performs detection using DSP algorithms. The digital system also allows the data to be integrated synchronously with the SMAP radar pulse-repetition interval (PRI) of approximately 350 μs. The types of algorithms implemented within the RDE are suggested by the earlier techniques used to identify RFI. The RDE outputs data that are sufficient for the ground science algorithm (described in Section IV) to compute the full Stokes vector and kurtosis for V and H polarizations within the 24-MHz full-band channel and 16 1.5-MHz subband channels. The kurtosis approach (see Section IV-A3) is used in an RFI detection algorithm based on a test of Gaussianity of the received signals, and requires knowledge of the first four signal moments. Accordingly, the RDE includes systems for computing and recording these moments.

The system consists of two analog processing units (APU) and one digital processing unit (DPU). The APU cards, one for each antenna polarization, are mixed-signal cards containing analog-to-digital converters that synchronously digitize radiometer signals at 96 megasamples per second (MSPS) and a resolution of 14 bits. The APU cards are interfaced to the DPU via a high-speed digital backplane card. The DPU performs additional signal processing functions and coordinates all radiometer control and command functions, data processing, and data packetization. Although microwave radiometry is frequently performed using a much smaller number of bits in the analog-to-digital conversion, the concern over RFI motivated the use of 14 bits in the SMAP conversion. The use of 14 bits allows the system to resolve small thermal noise contributions (which occupy only the lower 5–6 bits) while simultaneously avoiding nonlinearity and clipping caused by any large RFI sources that may be present [47].

A. SMAP DSP Architecture

The APU and DPU cards make up the heart of the RDE and form a field-programmable gate array (FPGA)-based digital signal processor (see Fig. 5). Radiation-tolerant FPGAs are used to make the system robust to failures that are potentially caused by in-orbit radiation effects. On each APU, the radiometer signal is digitized and has its dc offset removed by the signal preprocessing module. Next, the signal is processed through three major modules consisting of a digital downconverter, a 16-channel filter bank, and a statistics calculation unit (SCU). Each of these three modules resides in its own FPGA. Downconverted signals are called full-band signals, and the full-band signals that have been processed by the filter bank are called subband signals. The APU cards compute the first

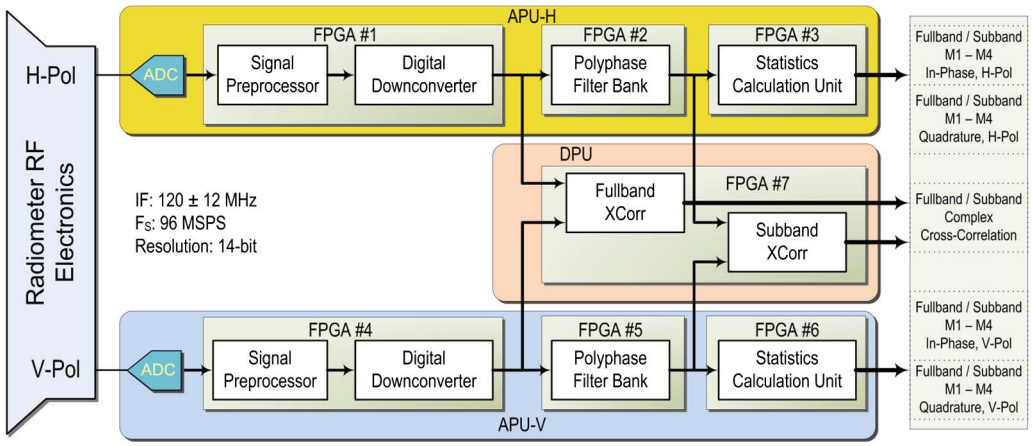

Fig. 5. SMAP DSP block diagram showing the seven FPGAs that perform signal processing and form output data products.

four raw sample moments of the full-band and subband signals. The first two moments are used to estimate antenna brightness temperature, whereas the first to fourth sample moments are used to estimate the kurtosis for each integration period. The output signals of the digital downconverter (DDC) and the filter bank for each APU are also routed over the backplane to the DPU, where their complex correlation coefficient is computed to form full-band and subband data products that are used for the third and fourth Stokes parameter measurements.

1) DDC: The digitized radiometer signal has approximately 24 MHz of bandwidth centered at 24 MHz when it reaches the RDE and is sampled at 96 MSPS. For a single polarization, the real-valued samples from the analog-to-digital converter are downconverted to baseband using quadrature downconversion. This process shifts the signal from real-valued data occupying 12–36 MHz to complex data occupying −12–12 MHz. A 63rd-order low-pass filter is applied to eliminate the image spectrum following the downconversion, and the data are decimated by a factor of 4 similar to the technique described in [12]. The resultant full-band complex output signal (sampled at 24 MSPS and occupying −12–12 MHz) is sent to the filter bank and the complex correlator in the RDE. The DDC was designed with on-orbit programmable low-pass filter coefficients so that the frequency response of the radiometer can be adjusted during the mission via commands from the ground. The coefficients are quantized to 12 bits to provide at most 60 dB of OOB attenuation. The default configuration consists of a 63rd-order Taylor window design that has at least 50 dB of stopband attenuation.

2) Polyphase Filter Bank: The radiometer science algorithm uses joint time–frequency diversity to aid in localizing intermittent RFI during the mission. The instrument accomplishes this through the use of a filter bank to separate the incoming complex full-band data into 16 frequency channels. The filter bank is implemented using a standard 16-channel polyphase filter bank approach [33], [34]. The filter bank is designed with periodically time-varying coefficients, so that all 16 subband channels can share the same processing engine, thereby drastically reducing the amount of FPGA logic that is otherwise required for implementation [35]. Similar to the DDC, the filter bank uses a 63rd-order polyphase filter, but it also employs a custom pipelined fast Fourier transform to separate the aliases of each channel. The frequency response of each channel is identical since a single prototype filter is shared among the 16 channels to make the subband signals. The channel response can be modified in-orbit as well as via a reprogrammable set of coefficients similar to the DDC design. The filter design is also quantized to 12 bits. The default configuration for the filter-bank prototype consists of a Taylor window design providing at least 42 dB of stopband attenuation per subband and 638 kHz of transition bandwidth (see Fig. 6). Furthermore, each channel was designed to overlap with its two adjacent channels, as is normally found in spectrum analyzer applications of filter banks [36]. As shown in Fig. 6, the filter response is −2.745 dB at the "crossover" point (i.e., midpoint in frequency) between the adjacent channels.

3) Complex Cross Correlator: The radiometer also computes the complex cross-correlation coefficient between the V and H polarizations for measuring the third and fourth Stokes parameters. Both full-band and subband correlations are performed on the DPU. Subband cross correlations are computed for each of the 16 channels using a shared hardware complex multiplier. All subband signals are correlated separately from the full-band signals, using a highly multiplexed complex multiplier and data buffers to organize the samples from the interleaved subband signals.

4) SCU and Science Telemetry Output: The SCU computes the first four sample moments on every signal type processed in the RDE, namely, the in-phase and quadrature (i.e., real and imaginary) component signals of the full-band and 16 subband signals. Since the RFI detection algorithm also employs kurtosis, the first to fourth sample moments are computed in hardware. The sample moments are computed and sent to the ground, where they are subsequently centralized and standardized for computing detected power and kurtosis, as described in Section IV.

The outputs of the SCU and the complex cross correlator are packetized and communicated to the ground during periodic downlinks. SMAP Level 1B brightness-temperature products (described in Section IV) are computed at a time resolution of 15.4 ms. The RDE oversamples this reporting interval by 44 and 11 times for the full-band and subband moments, respectively. On the ground, Level 1B products are formed by the science

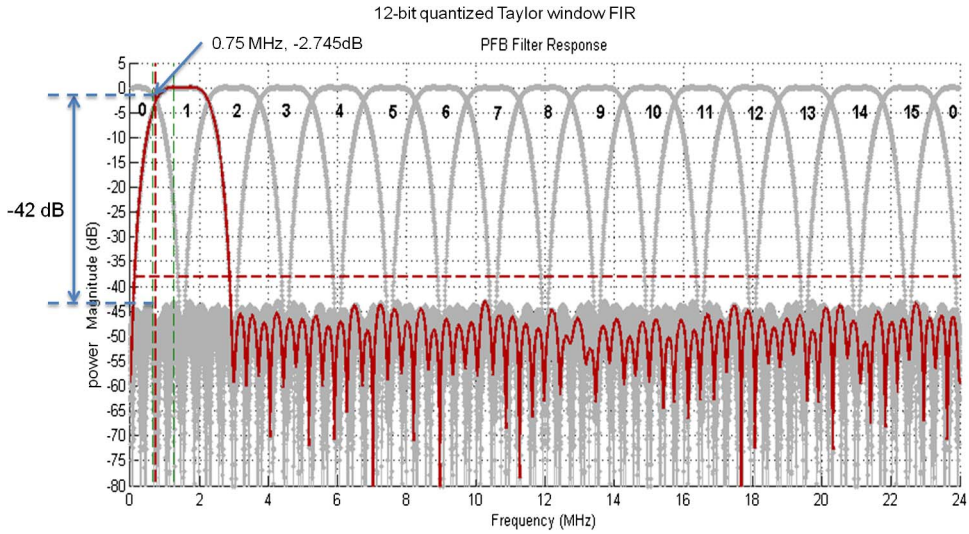

Fig. 6. Frequency response of the SMAP RDE filter bank.

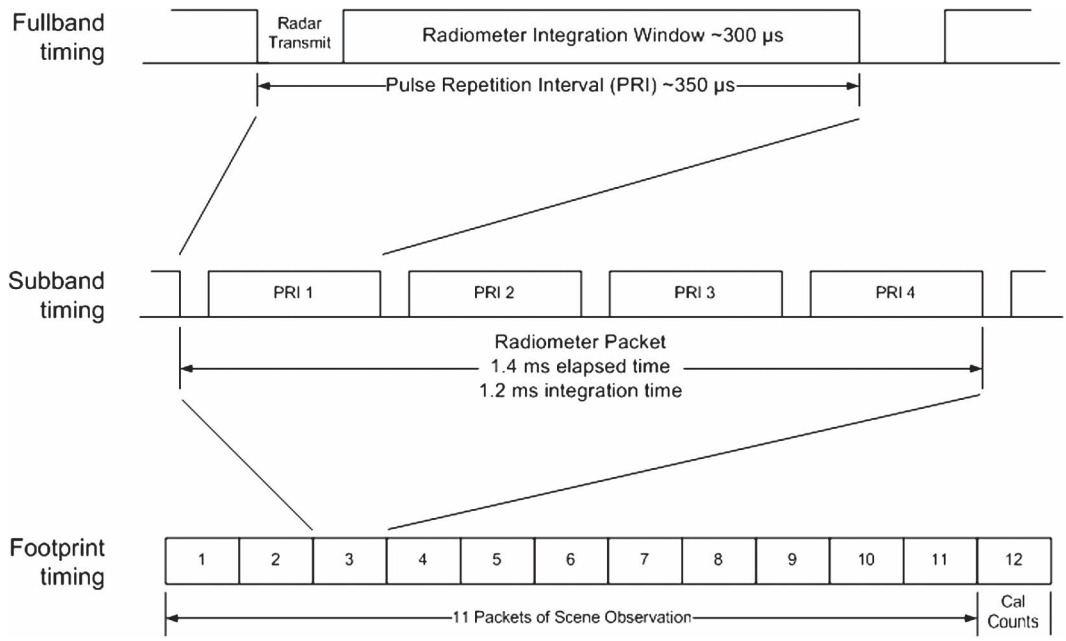

Fig. 7. Radiometer timing sequence. (From bottom to top) Level 1B brightness-temperature product is computed from 11 × 1.4-ms packets. Each packet contains subband measurements for 16 frequency channels at an integration time of 1.2 ms (elapsed time of 1.4 ms), and four full-band measurements representing the 4 × 300-μs integration time PRIs (4 × 350-μs elapsed time) comprising the 1.4-ms packet.

algorithm software by averaging multiple time–frequency moments. The sampling scheme is illustrated in Fig. 7. The total number of samples for an L1B product is shown in Table I. The cost of doing RFI mitigation is the collection of ∼1000 times more data than minimally required to measure the full Stokes antenna temperature vector. It is noted that a reduction in the amount of data would likely be possible by performing some of the RFI detection and mitigation on board the satellite, as described in [39] and [44], as opposed to in-ground processing. However, for the SMAP mission, even the large amount of data reported by the RDE remains modest as compared with the data downlink requirements of the coobserving SMAP radar system. The added flexibility of RFI detection and mitigation in ground processing, which allows postobservation modification of detection algorithms and thresholds, also motivates the strategy adopted.

IV. SMAP Radiometer RFI Algorithm

As shown earlier, the SMAP radiometer instrument provides a large amount of information that is telemetered from the satellite to enable the use of multiple RFI detection methods on the ground. Within the SMAP brightness-temperature ground algorithm, RFI mitigation (detection and removal) is performed after radiometric calibration and before conversion of antenna temperatures T_A to surface-referenced brightness temperatures [45]. The detection process comprises pulse, cross frequency, kurtosis, and polarization-anomaly detectors. The binary

TABLE I
MEASUREMENTS COLLECTED BY SMAP FOR A SINGLE PRODUCT TO ENABLE RFI DETECTION AND REMOVAL

Polarization or Stokes parameter	No. of freq. channels	Samples per product	Baseband I/Q components	Raw moments or cross correlations
Fullband Channels				
V	1	44	2	4
H	1	44	2	4
3	1	44	1	1
4	1	44	1	1
		Subtotal of measurements:		792
Subband Channels				
V	16	11	2	4
H	16	11	2	4
3	16	11	1	1
4	16	11	1	1
		Subtotal of measurements:		3168
	Total measurements for single product:			**3960**

outputs of the detectors are combined in a way to maximize the probability of detecting RFI within a product. Finally, the time–frequency samples determined to be RFI free are averaged to form a product.

The 15.4-ms reporting interval for a SMAP brightness-temperature product includes only 13.2 ms of antenna observation time (see Fig. 7). Given the 24-MHz bandwidth and a nominal system temperature of 540 K (assuming a scene brightness temperature of 250 K), a noise-equivalent delta temperature (NEDT) of 0.96 K results as the measurement uncertainty in a single brightness-temperature product before any RFI mitigation is performed.

A. RFI Detection Methods

The individual RFI detection algorithms operate on data samples with different time and frequency resolutions. Full-band measurements (covering the full 24-MHz passband) are available every 350 μs. From these measurements, full-band versions of each RFI flag are produced. Subband measurements (covering each of the 16 subbands with 1.5 MHz of bandwidth across the 24-MHz passband) are available every 1.4 ms. From these measurements, 16 separate subband versions of each RFI flag are produced.

Each of the detection algorithms has associated with it the statistical properties of its performance, i.e., a pdf for the variable on which the detection decision is based, and given a detection threshold (hereafter denoted β) to which that variable is compared, a probability of deciding RFI is present when it is not (i.e., the false-alarm rate or FAR) and a probability of detecting RFI is present when it is (i.e., the PD). The choice of threshold value determines where each detector will operate on the receiver operating curve (ROC), thus establishing its FAR and PD. With each detection algorithm, the value of β varies geographically via a lookup table with a $1^\circ \times 1^\circ$ resolution in latitude and longitude to account for variations in the likelihood and the type of RFI. A uniform prelaunch value for β is set so that the FAR causes an increase in the effective NEDT of the product average of only 5% when no RFI is present. This corresponds to a FAR of 9.3%. It is expected that the value used for β will be revisited after launch once the actual RFI environment has been characterized. For example, it may be prudent to increase the FAR in geographical regions subject to persistent RFI in order to improve the PD since widespread low-level RFI will be more likely to occur.

1) Time Domain or Pulse Detection: The time-domain or pulse detection algorithm searches in time for increased levels of observed antenna temperatures above those produced by normal statistical behavior [12], [37]. The algorithm is also referred to as asynchronous pulse blanking since no periodic properties of the RFI are assumed. This detection method is best suited to detect impulsive RFI with large amplitudes and short duration or low duty cycles, i.e., properties inherent to one of the main RFI sources observed at L-band (air surveillance radar systems). This detection method is applied within a product containing 44 samples of full band T_A's for both the V and H polarizations. RFI detection occurs when

$$T_A - m \geq \beta_{\mathrm{td}} \sigma_{\mathrm{td}} \tag{2}$$

where m is the mean of a predetermined window of T_A samples without the largest 10% of samples to avoid biasing from RFI, and σ_{td} is the standard deviation of those samples. This window contains samples from the product under observation and samples from previous and succeeding products.

2) Cross-Frequency Detection: The cross-frequency detection algorithm is similar to the pulse detection algorithm, except that it searches for increased levels of antenna temperatures that are recorded in multiple frequency channels [38], [39]. The inputs to the cross-frequency algorithm are subband antenna temperatures for both V and H polarizations. The passband is divided into 16 subbands, and the science data contain samples that are integrated over four consecutive PRIs (a total of 1.4 ms) for each subband (see Fig. 7). The cross-frequency algorithm operates on a single time subsample of 16 frequency subbands at a time. For each time subsample, RFI detection occurs similarly to (2). For a given integration period, the average of 16-N channels with the smallest T_A values is used to estimate the mean and the standard deviation of the frequency subbands. A value of $N = 4$ is used as the change in the mean is less than 2 K if RFI is absent. Any channel that contains T_A's that are β_{cf} standard deviations above the mean is flagged as corrupted and then removed. Subbands adjacent to those flagged as containing RFI are also flagged as corrupted and are then removed. The SMAP algorithms currently include two cross-frequency approaches operating at the original time resolution (1.4 ms) and operating after integration to the product scale (15.4 ms). The latter detection method in particular has been shown to be more sensitive to CW RFI.

3) Kurtosis Detection: The kurtosis detection algorithm detects the presence of RFI using the kurtosis statistic [13], [40], [41]. The kurtosis statistic, which is used in standard tests for normality [32], is computed from the first four raw moments of the radiometer signal voltage x, i.e.,

$$K = \frac{\left\langle (x - \langle x \rangle)^4 \right\rangle}{\left\langle (x - \langle x \rangle)^2 \right\rangle^2} \tag{3}$$

where $\langle\rangle$ denotes the expected value operator. It is the fourth central moment of x divided by the square of its second central moment. Both the numerator and the denominator of (3) can be expanded in terms of the individual moments of x

$$K = \frac{m_4 - 4m_1m_3 + 6m_1^2m_2 - 3m_1^4}{(m_2 - m_1^2)^2} \tag{4}$$

where $m_n = \langle x^n \rangle$ is the nth raw (i.e., not central) moment of x. Equation (4) is used to compute the kurtosis from the individual raw moments that are actually measured by SMAP.

The inputs to the kurtosis algorithm are samples of the first four raw moments that are used prior to any time or frequency averaging, i.e., with the shortest integration time and from each individual frequency and polarization subband and full-band channel. Equation (4) is used separately on both I and Q components of the baseband signal for each frequency subband (includes full band) and each radiometer channel (V and H).

The nominal Gaussian-distributed kurtosis value for each radiometer channel is determined in prelaunch testing. This is the value from which deviations are computed to identify RFI. The value is ideally equal to 3 for a continuous system, but quantization effects lower the actual value. Additionally, the kurtosis threshold, which is the deviation from the nominal kurtosis value beyond which a sample is considered corrupted by RFI, for each channel is determined during prelaunch testing. As with the previous two detectors, the value of this threshold determines the FAR and PD of RFI. For each time and frequency subsample, the value of the kurtosis is compared with the nominal Gaussian value, and detection occurs if the deviation from the nominal value exceeds the following threshold:

$$|K - K_{\rm nom}| > \beta_K \sigma_K \tag{5}$$

where K is the measured kurtosis, $K_{\rm nom}$ is the *a priori* nominal kurtosis value, β_K is the threshold value that determines the FAR, and σ_K is the standard deviation of the measured kurtosis. As mentioned previously, threshold β_K will in general depend on latitude and longitude, as defined by a lookup table with a $1^\circ \times 1^\circ$ resolution, and will be set prior to launch based on a preset FAR. Initial values for σ_K are determined by prelaunch measurements but may change on orbit due to instrument aging. For the case of the frequency subband channels, RFI is additionally flagged as being present in both subbands adjacent to the subband in which RFI is actually detected.

4) Polarization Detection: The detection algorithm which uses the third and fourth Stokes parameters (T_3 and T_4, respectively) is a simple thresholding algorithm that searches for variations greater than a fixed number of standard deviations away from reasonable geophysical values, which has been shown to be valuable for identifying RFI in SMOS measurements [28]. In general, RFI detection occurs when

$$|T_{3,4} - T_{\rm nom}| \geq \beta_{3,4}\sigma_{3,4} \tag{6}$$

where $\beta_{3,4}$ is the threshold multiplier, and $\sigma_{3,4}$ is the standard deviation of the third or fourth Stokes parameter in antenna temperature. Equation (6) is performed on both the time- (full-band) and frequency-domain (subband) data and for third and fourth Stokes parameters, separately.

For the fourth Stokes parameter, the $T_{\rm nom}$ value is expected to be zero over a land area and to be small over the ocean; although at shorter wavelengths, large values of both third and fourth Stokes parameters have been observed over the Greenland ice sheet [42]. Nonetheless, SMAP data are flagged for RFI when

$$|T_4(T)| \geq \beta_4\sigma_4. \tag{7}$$

The third Stokes parameter will be nonzero in the presence of ionospheric Faraday rotation. Assuming no third Stokes is generated by the Earth's surface [43], we have

$$T_3' = (T_h - T_v)\sin 2\varphi \tag{8}$$

where φ is the Faraday rotation angle. There are several options for detecting RFI with the third Stokes parameter. For example, $T_{\rm nom}$ could be determined using a model for T_3' due to Faraday rotation and measured anomalies tested against the threshold. A greatly simplified approach would be to take $T_{\rm nom} = 0$ and use an expanded value for $\beta_3\sigma_3$ to account for the expected range of T_3' This approach should work well particularly during the *ante meridiem* portion of the orbit when the total electron content in the ionosphere is low, at the cost of a reduced sensitivity in RFI detection.

B. RFI Removal Using MPD

Each of the above detectors is sensitive to different kinds of RFI. A single maximum PD (MPD) flag, which minimizes the probability of missing the detection of RFI, is formed by a logical OR operation of each of the individual RFI detector outputs. Due to the logical OR operation, no RFI detected by any individual algorithm can be missed by the MPD algorithm. For this reason, the MPD flag minimizes the probability of missed detection; in other words, the PD is maximized given the available individual detectors.

Two versions of the MPD algorithm are implemented in the ground software: a full-band version operating on the 350-μs samples and a 16-subband version operating on 1.4-ms samples. The philosophy of using a logical OR operation to combine individual flags is used to combine the outputs of the two versions in the following manner. If a full-band MPD flag is set high (indicating the presence of RFI), then all 16 subbands that include that time interval are considered contaminated with RFI. This methodology is illustrated in Fig. 8. RFI removal is accomplished by including in the final product average (over the 11 time samples by the 16-subchannel spectrogram) only those second moment subband counts for which the composite MPD flag is not set.

The SMAP brightness-temperature science product (L1B_TB) includes T_A before RFI mitigation, T_A after RFI mitigation, and the estimated NEDT for the T_A of each product after RFI mitigation. The L1B_TB product also contains a 2-bit RFI flag for each product that indicates the

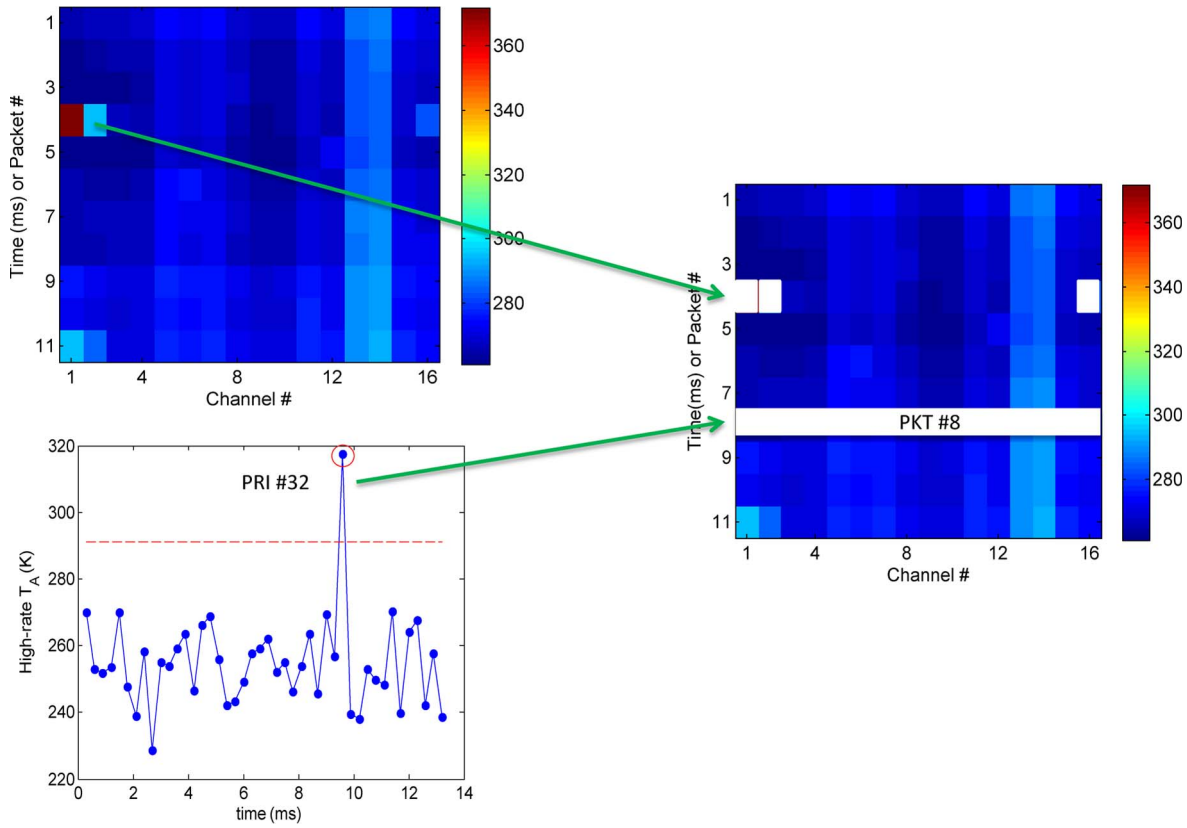

Fig. 8. Example of the MPD operation. The top left plot shows the pulse detection algorithm detecting RFI in the time domain, and the right plot shows that the corresponding time slice in the time–frequency data is flagged for removal. The cross-frequency algorithm detects RFI in the time–frequency data shown on the bottom left and that pixel, in addition to the pixels of adjacent channels, are flagged for removal. All time- and frequency-domain detection methods similarly flag pixels in the time–frequency data for removal. The remaining clean pixels are then averaged to form a product.

quality of the T_A for that product, as well as a flag indicating the quality of the associated NEDT. The RFI flag specifies if the individual T_A is RFI free and no correction was necessary (i.e., none of the detectors indicated that RFI was present), if RFI was detected and removed, or if RFI was detected but not removed. The RFI removal algorithm does not in principle limit the amount of data that can be discarded before combining to form an RFI-free T_A for an individual product. However, a threshold on the amount of data discarded is set beyond which RFI mitigation is not attempted. The NEDT is estimated from the RFI-free time–frequency samples averaged to produce a measurement. The quality flag for the associated NEDT is a one-bit flag indicating whether the resulting NEDT is acceptable or too high based on a predetermined threshold that meets science requirements.

V. ETU Testing

The SMAP radiometer ETU was developed to verify system performance, including RFI detection and mitigation, in preflight test activities. The ETU includes fully functional radiometer RF and digital electronics (with the exception of the antenna), and operates in a manner identical to the flight unit. Numerous tests of system performance with the ETU have been performed; examples involving RFI detection and mitigation are described here.

A. Test Setup

RFI performance tests with the ETU were conducted by coupling a known brightness-temperature source, $T_{B,\mathrm{load}}$ into the radiometer input. Additional RFI test signals $T_{B,\mathrm{rfi}}$ were combined with this thermal noise input, and measurements were performed with the RFI signals turned on or off in order to clarify RFI contributions. Injected RFI signals were primarily of the pulsed-sinusoidal type in the results reported here and included four different pulsewidths (2, 30, and 450 μs, and continuous) at a fixed 596-Hz pulse repetition frequency (PRF) (1.68-ms PRI). A variety of pulse amplitudes and frequencies was utilized, with the goal of spanning low-level (0.1 K) to high-level (1000 K) $T_{B,\mathrm{rfi}}$ contributions.

The ground processing software reports brightness temperatures both before (T_{meas}) and after (T'_{meas}) RFI mitigation algorithms are applied. If, for example, only a thermal noise source is present, we label T_{meas} as T_{load} (no mitigation) and T'_{meas} as T'_{load}. In this case, $B = T_{\mathrm{load}} - T'_{\mathrm{load}}$ represents a bias in the measurement caused by false alarms. Because this bias is fixed for constant $T_{B,\mathrm{load}}$, it can be estimated by averaging over many RFI-free measurements (denoted as $\langle B \rangle$) and compensated whenever RFI mitigation is performed. Note that T_{load} remains a better estimate of the true thermal noise brightness $(T_{B,\mathrm{load}})$ than $T'_{\mathrm{load}} + \langle B \rangle$ in the absence of RFI since T_{load} is not subject to any variations induced by false alarms in the mitigation process.

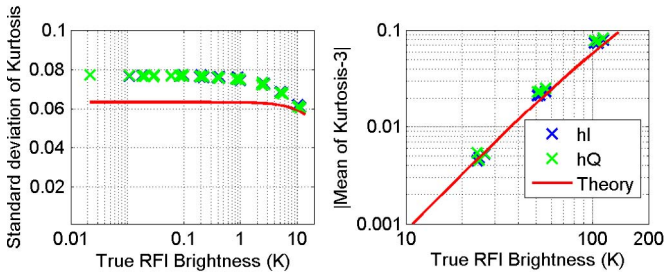

Fig. 9. (Left) Standard deviation and (right) mean of the full-band kurtosis in the presence of injected sinusoidal RFI of the brightness temperature given on the horizontal axis. Measured data for both the I and Q channels (labeled "hI" and "hQ" respectively) of H polarization are shown.

With RFI injected, we label $T_{\rm meas}$ as $T_{\rm load+rfi}$ and $T'_{\rm meas}$ as $T'_{\rm load+rfi}$. An estimate of the true RFI present $T_{B,\rm rfi}$ is $T_{\rm load+rfi} - T_{\rm load}$, and an estimate of the induced bias following mitigation is $T'_{\rm load+rfi} + \langle B \rangle - T_{\rm load}$.

Because it is important to characterize detection and mitigation performance for RFI levels as small as 0.1 K, a procedure was required to allow the measurement of brightness temperatures to this accuracy (recall that the 15.4-ms SMAP L1B product NEDT is 0.96 K). Accordingly, measurements in each radiometer state (i.e., with a given RFI signal turned on or off) were performed for a duration of 18.48 s (1200 SMAP L1B_TB products). The corresponding NEDT of the 1200 product average is 34.6 times smaller (0.03 K) than that of a single product, allowing examination of the small RFI-induced errors in the mitigated averaged products (i.e., the average of $T'_{\rm load+rfi} + \langle B \rangle - T_{\rm load}$).

Changes in NEDT associated with mitigation can be also computed by comparing the standard deviation of the mitigated products (estimated using the 1200 data points in a given state) to the RFI-free unmitigated case.

B. Example Test Results

1) Full-Band Kurtosis Measurement: As a first example of system measurement of the full-band kurtosis, Fig. 9 plots the mean and standard deviation of the full-band kurtosis (at 350-μs time resolution) in the presence of injected sinusoidal RFI. Results are shown in both the I and Q channels of H polarization, and they show the small variations in full-band kurtosis that occur in the presence of CW interference. Nine differing in-band RFI frequencies are included, at a variety of power levels of up to more than 100 K. The results for the mean show a good match to the theory of such measurements [40], whereas the measured standard deviations are moderately higher than those predicted by the theory. A further analysis showed that these increases arise from the discretization level of the fourth signal moment, which can be reduced by modification of the digital back-end parameters. The kurtosis values observed are less than the nominal value of 3 for sinusoidal interference (only the absolute value of the deviation is shown in the right plot in Fig. 9) but become larger than 3 for pulsed interference. The ability of the radiometer to measure the kurtosis therefore provides some measure of RFI classification and detection. Similar analyses were performed for pulsed interference sources of varying duty cycles, and a reasonable match to the theory [40] was observed.

2) Cross-Frequency Mitigation: Fig. 10 illustrates a sample calibrated spectrogram (11 time samples by 16 frequency channels) corresponding to a single SMAP L1B_TB product in V polarization. Continuous sinusoidal RFI at frequency of 1413.5 MHz (the center of the SMAP passband) is injected, in this example, at a power level of 17.3 K larger in the center channel, as compared with the other channels. This RFI level corresponds to an increase of 1.08 K in the integrated measurement. The left plot illustrates the RFI corrupted spectrogram and shows the clear presence of the RFI at its true frequency location. The right plot shows the same spectrogram following blanking by the SMAP mitigation algorithms. In this low-level continuous RFI case, no detections occur in the full-band algorithms (thresholds are set to a low FAR in this example). The kurtosis and cross-frequency detectors over the spectrogram show some false alarms (the isolated points in the spectrogram), whereas the cross-frequency algorithm at a resolution of 15.4 ms removes the corrupted frequency channel and adjacent channels entirely. The result is that 46 out of 176 measurements are discarded to mitigate the RFI, which results in a 16.3% increase in NEDT. The corresponding mitigated brightness averaged over many measurements in this state is 114.6 K, as compared with the RFI-free brightness temperature of 114.7 K. Similar measurements were performed at a variety of power levels and frequencies of injected CW RFI; the initial results show that CW RFI can be detected and mitigated at power levels ranging from less than 1 K up to more than 100 K.

3) Removal of Pulsed RFI: Fig. 11 plots sample-calibrated full-band products (V polarization) that include a 2-μs pulsewidth RFI source with a PRF of 596 Hz at two differing power levels (a contribution of 3.84 K to integrated brightness temperature in the upper row and 1.74 K in the lower). The time interval shown (44 $\times$ 350-μs samples) corresponds to the subsamples in one 15.4-ms SMAP L1B_TB product. The source pulses of higher amplitude are readily distinguishable in the brightness temperature time history (upper left) but are less distinguishable at lower amplitudes (lower left). The corresponding full-band kurtosis measurements are shown in the right plots (note that the kurtosis in the vertically polarized I and Q channels is averaged). Again, the outliers are obvious at higher amplitudes but are less obvious, although still present, at lower amplitudes. The time history plots include markers indicating samples detected by the combined pulse and kurtosis detectors. The original and mitigated brightness temperatures computed from the full-band products are 120.01 and 116.15 K (after 0.19-K bias correction), respectively, in the higher amplitude case, so that 3.86 K is mitigated as compared with the true RFI brightness temperature of 3.84 K. In the lower RFI brightness-temperature case, the original and mitigated brightness temperatures are 117.75 and 117.12 K, so that only 0.63 K, as compared with the true RFI brightness temperature of 1.74 K, is mitigated. The latter represents an uncorrected RFI bias of 1.11 K. However, the current SMAP processor computes output brightness temperatures from full-band measurements only over ocean regions. As discussed previously, full-band

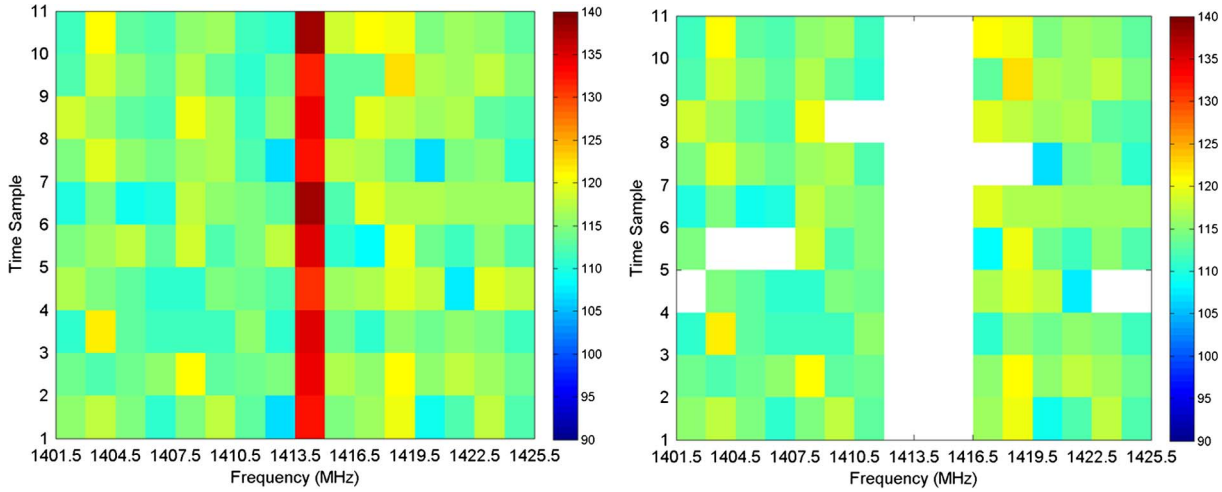

Fig. 10. Time–frequency 11 × 16 calibrated vertically polarized spectrograms from the SMAP ETU containing injected continuous sinusoidal RFI at frequency of 1413.5 MHz. The left plot shows the original spectrogram, and the right plot includes masking by RFI detection algorithms.

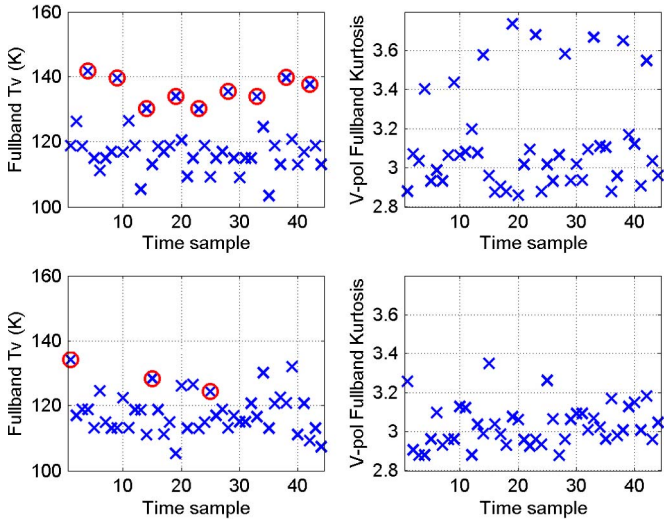

Fig. 11. Example full-band measurements (V polarization) containing injected 2-μs pulsed RFI at PRF of 596 Hz. The upper plots are examples with source amplitude corresponding to a bias of 3.84 K in the final brightness temperatures, and the lower plots have an amplitude of 1.74 K. The left plots are the full-band power history, whereas the right plots illustrate the corresponding full-band kurtosis. Points in the left plots marked with circles are detected by full-band pulse or kurtosis algorithms.

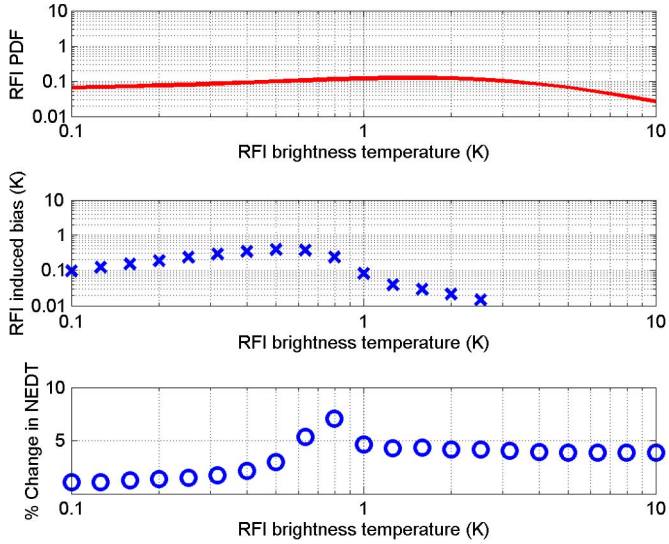

Fig. 12. Procedure for estimating global SMAP performance. (Middle and lower plots) SMAP radiometer performance simulations can be multiplied by (upper plot) SMOS RFI pdf and integrated over the RFI brightness temperature to estimate a global expected value of the RFI impact on SMAP measurements.

measurements serve only to provide flags in the spectrogram integration over land regions. Improved performance in detecting even the lower amplitude source is achieved by the kurtosis and cross-frequency detectors in the spectrogram. However, the current full-band flagging process results in a large percentage of the spectrogram being discarded since nearly all 1.4-ms intervals contain a pulse detected by the full-band algorithms. Additional refinements to the SMAP processing algorithms to allow the use of full-band products in computing the brightness temperature over land in some situations are currently under consideration.

4) Simulated Results: Although preflight testing to predict the overall impact of RFI on SMAP science products continues, initial simulated results, as shown in Fig. 12, are available that illustrate the concept for applying the RFI environment description in SMAP performance assessment. The solid curve in the upper plot of Fig. 12 is the pdf of RFI brightness temperatures derived from the SMOS analysis of Section II (the same as in Fig. 4). As shown earlier, this pdf shows significant RFI presence over a wide range of source brightness temperatures, including an almost uniform distribution of low-level cases that will be challenging for detection and mitigation. The middle plot in Fig. 12 represents simulated biases $(T'_{\mathrm{load+rfi}} + \langle B \rangle - T_{\mathrm{load}})$ of SMAP radiometer measurements with respect to the true geophysical brightness in the presence of RFI of a specified brightness temperature (horizontal axis), following the application of SMAP radiometer detection and mitigation algorithms. For example, the "low amplitude" measurement presented in Section V-B3 had an RFI brightness temperature of 1.74 K (horizontal axis) and resulted in a post-mitigation bias of 1.11 K (vertical axis). The curve shown in the

middle plot was obtained from simulations (not measurements) of the SMAP radiometer detection and mitigation algorithms for a particular pulsed source type for which detection and mitigation performance was improved, as compared with the example in Section V-B3, so that a bias of less than 0.1 K occurs for true RFI level of 1.74 K. The lower plot in Fig. 12 is a similar illustration from the simulations of the percentage increase in the radiometer NEDT that occurs following RFI mitigation. These curves can be computed for a specified RFI source type, could be recomputed for many RFI source types, and can be replaced in the future with measured data such as that from the ETU. An integration of such results over the RFI pdf can provide a global estimated value for the bias caused by RFI (of a given type), which can be then assessed against the SMAP error budget.

VI. Discussion and Plan Forward

The SMAP radiometer and ground algorithms are designed to detect and remove the widespread RFI evident in measurements obtain from the recent spaceborne radiometers on Aquarius and SMOS. Using observations collected with ground- air- and space-based systems, the RFI environment to be experienced by SMAP is characterized and found to contain a substantial amount of low-level RFI with varying time–frequency characteristics. Both impulsive interference due to OOB emissions from radar systems and narrow-band spurious emissions from communications invade the protected spectrum to be utilized by SMAP. To enable RFI detection and removal on the ground, the SMAP flight system produces almost 1000 times more measurements than would be otherwise required in a conventional system. A digital detector back end is implemented to output the first four raw moments and complex cross correlation of the received signals in both V and H polarizations across 16 channels. These data are used on the ground to detect RFI in the time, frequency, statistics, and polarization domains. Using a wide variety of detectors enables SMAP to differentiate between the desired thermal emission and harmful interference. Detector thresholds are set prior to launch for a 9.3% FAR, which results in negligible NEDT degradation. After launch and once the RFI environment is characterized, threshold values will be adjusted for each detector on a geographic basis to optimize the mitigation results. The operation of the hardware and utility of the ground software are demonstrated with the SMAP radiometer ETU and the prototype algorithm. Additional testing continues with the ETU and, ultimately, the flight model hardware for full performance verification.

References

[1] D. Entekhabi, E. G. Njoku, P. E. O'Neill, K. H. Kellogg, W. T. Crow, W. N. Edelstein, J. K. Entin, S. D. Goodman, T. J. Jackson, J. Johnson, J. Kimball, J. R. Piepmeier, R. D. Koster, N. Martin, K. C. McDonald, M. Moghaddam, S. Moran, R. Reichle, J.-C. Shi, M. W. Spencer, S. W. Thurman, and J. Van Zyl, "The Soil Moisture Active Passive (SMAP) mission," *Proc. IEEE*, vol. 98, no. 5, pp. 704–716, May 2010.

[2] C. D. Crandall, Survey of potential radio frequency interference sources, Space Comm. Tech. Dir., Naval Res. Lab., Washington, DC, USA, Memo. Rep. NRL-MR-4200. [Online]. Available: torpedo.nrl.navy.mil/tu/ps/doc.html?dsn=352081

[3] L. Li, E. G. Njoku, E. Im, P. S. Chang, and K. St. Germain, "A preliminary survey of radio-frequency interference over the U.S. in Aqua AMSR-E data," *IEEE Trans. Geosci. Remote Sens.*, vol. 42, no. 2, pp. 380–390, Feb. 2004.

[4] E. G. Njoku, P. Ashcroft, T. K. Chan, and L. Li, "Global survey and statistics of radio-frequency interference in AMSR-E land observations," *IEEE Trans. Geosci. Remote Sens.*, vol. 43, no. 5, pp. 938–947, May 2005.

[5] L. Li, P. W. Gaiser, M. H. Bettenhausen, and W. Johnston, "WindSat radio-frequency interference signature and its identification over land and ocean," *IEEE Trans. Geosci. Remote Sens.*, vol. 44, no. 3, pp. 530–539, Mar. 2006.

[6] S. Mecklenburg, M. Drusch, Y. H. Kerr, J. Font, M. Martin-Neira, S. Delwart, G. Buenadicha, N. Reul, E. Daganzo-Eusebio, R. Oliva, and R. Crapolicchio, "ESA's soil moisture and ocean salinity mission: Mission performance and operations," *IEEE Trans. Geosci. Remote Sens.*, vol. 50, pt. 1, no. 5, pp. 1354–1366, May 2012.

[7] *Handbook of Frequency Allocations and Spectrum Protection for Scientific Uses*, National Research Council of the National Academies, The National Academies Press, Washington, DC, USA, 2007.

[8] G. Lagerloef, F. R. Colomb, D. Le Vine, F. Wentz, S. Yueh, C. Ruf, J. Lilly, J. Gunn, Y. Chao, A. deCharon, G. Feldman, and C. Swift, "The aquarius/SAC-D mission: Designed to meet the salinity remote-sensing challenge," *Oceanography*, vol. 21, no. 1, pp. 68–81, Mar. 2008.

[9] J. R. Piepmeier and F. Pellerano, "Mitigation of terrestrial radar interference in L-band spaceborne microwave radiometers," in *Proc. IEEE IGARSS*, Denver, CO, USA, Jul. 30/Aug, 4, 2006, pp. 2292–2296.

[10] S. Misra and C. S. Ruf, "Detection of radio frequency interference for the Aquarius radiometer," *IEEE Trans. Geosci. Remote Sens.*, vol. 46, no. 10, pp. 3123–3128, Oct. 2008.

[11] C. S. Ruf, D. Chen, D. LeVine, P. deMatthaeis, and J. R. Piepmeier, "Aquarius radiometer RFI detection, mitigation, and impact assessment," in *Proc. IEEE IGARSS*, Munich, Germany, Jul. 2012, pp. 3312–3315.

[12] N. Niamsuwan, J. T. Johnson, and S. W. Ellingson, "Examination of a simple pulse blanking technique for RFI mitigation," *Radio Sci.*, vol. 40, no. 5, pp. RS5S03-1–RS5S03-5, Oct. 2005.

[13] C. S. Ruf, S. M. Gross, and S. Misra, "RFI detection and mitigation for microwave radiometry with an agile digital detector," *IEEE Trans. Geosci. Remote Sens.*, vol. 44, no. 3, pp. 694–706, Mar. 2006.

[14] J. T. Johnson and J. R. Piepmeier, "Radio frequency interference and the SMAP radiometer: Risk assessment and reduction," presented at the Proc. IEEE IGARSS, Honolulu, HI, USA, 2010, Paper TH3.L10.3.

[15] M. Spencer, S. Chan, E. Belz, J. Piepmeier, P. Mohammed, E. Kim, and J. T. Johnson, "Radio frequency interference mitigation for the planned SMAP radar and radiometer," in *Proc. IEEE IGARSS*, Vancouver, BC, Canada, 2011, pp. 2440–2443.

[16] C. Chen, J. R. Piepmeier, J. T. Johnson, and H. Ghaemi, "Assessment of the impacts of radio frequency interference on SMAP radar and radiometer measurements," in *Proc. IEEE IGARSS*, Munich, Germany, 2012, pp. 1–4.

[17] J. R. Piepmeier, M. Midon, A. Caroglanian, and O. Ugweje, "Radio frequency survey of the 21 cm (1.4 GHz) allocation for passive microwave observing," in *Proc. IEEE IGARSS*, Toulouse, France, 2003, pp. 1739–1741.

[18] N. Niamsuwan and J. T. Johnson, "Sky observations at L-band using an interference suppressing radiometer," in *Proc. IEEE IGARSS*, Seoul, Korea, 2005, pp. 5562–5565.

[19] J. Park, J. T. Johnson, N. Majurec, N. Niamsuwan, J. R. Piepmeier, P. N. Mohammed, C. S. Ruf, S. Misra, S. H. Yueh, and S. J. Dinardo, "Airborne L-band RFI observations from the SMAPVEX08 campaign and associated flights," *IEEE Trans. Geosci. Remote Sens.*, vol. 49, no. 9, pp. 3359–3370, Sep. 2011.

[20] N. Skou, S. Misra, J. E. Balling, S. S. Kristensen, and S. S. Sobjaerg, "L-band RFI as experienced during airborne campaigns in preparation for SMOS," *IEEE Trans. Geosci. Remote Sens.*, vol. 48, no. 3, pp. 1398–1407, Mar. 2010.

[21] P. Fanise, M. Parde, M. Zribi, M. Dechambre, and C. Caudoux, "Analysis of RFI identification and mitigation in CAROLS radiometer data using a hardware spectrum analyzer," *Sensors*, vol. 11, no. 3, pp. 3037–3050, Mar. 2011.

[22] Y. H. Kerr, P. Waldteufel, J.-P. Wigneron, S. Delwart, F. Cabot, J. Boutin, M.-J. Escorihuela, J. Font, N. Reul, C. Gruhier, S. E. Juglea, M. R. Drinkwater, A. Hahne, M. Martin-Neira, and S. Mecklenburg, "The SMOS mission: A new tool for monitoring key elements of the global water cycle," *Proc. IEEE*, vol. 98, no. 5, pp. 666–687, May 2010.

[23] "Special issue on Soil Moisture and Ocean Salinity (SMOS) mission," *IEEE Trans. Geosci. Remote Sens.*, vol. 50, pt. 1, no. 5, May 2012.

[24] E. Anterrieu, "On the detection and quantification of RFI in L1A signals provided by SMOS," *IEEE Trans. Geosci. Remote Sens.*, vol. 49, no. 10, pp. 3986–3992, Oct. 2011.
[25] R. Oliva, E. Daganzo, Y. H. Kerr, S. Mecklenburg, S. Nieto, P. Richaume, and C. Gruhier, "SMOS RFI scenario: Status and actions taken to improve the RFI environment in the 1400-1427 MHz passive band," *IEEE Trans. Geosci. Remote Sens.*, vol. 50, no. 5, pp. 1427–1440, May 2012.
[26] R. Castro, A. Gutierrez, and J. Barbosa, "A first set of techniques to detect RFI and mitigate their impact on SMOS data," *IEEE Trans. Geosci. Remote Sens.*, vol. 50, no. 5, pp. 1440–1447, May 2012.
[27] A. Camps, J. Gourrion, J. M. Tarongi, M. Vall-Llossera, A. Gutierrez, J. Barbosa, and R. Castro, "RFI detection and mitigation algorithms for synthetic aperture radiometers," *Algorithms*, vol. 4, no. 3, pp. 155–182, Aug. 2011.
[28] S. Kristensen, J. E. Balling, N. Skou, and S. S. Sobjaerg, "RFI in SMOS data detected by polarimetry," in *Proc. IEEE IGARSS*, Munich, Germany, 2012, pp. 3320–3323.
[29] S. M. Misra and C. S. Ruf, "Analysis of radio frequency interference detection algorithms in the angular domain for SMOS," *IEEE Trans. Geosci. Remote Sens.*, vol. 50, no. 5, pp. 1448–1457, May 2012.
[30] A. J. Camps, I. Corbella, F. Torres, J. Bara, and J. Capdevila, "RF interference analysis in aperture synthesis interferometric radiometers: Application to L-band MIRAS instrument," *IEEE Trans. Geosci. Remote Sens.*, vol. 38, no. 2, pp. 942–950, Mar. 2000.
[31] M. Aksoy and J. T. Johnson, "A comparative analysis of low-level radio frequency interference in SMOS and Aquarius microwave radiometer measurements," *IEEE Trans. Geosci. Remote Sens.,* [Online]. Available: http://ieeexplore.ieee.org/xpl/articleDetails.jsp?arnumber=6555899
[32] M. G. Kendall and A. Stuart, *The Advanced Theory of Statistics*. New York, NY, USA: Hafner, 1996.
[33] L. R. Rabiner, *Multirate Digital Signal Processing*. Upper Saddle River, NJ, USA: Prentice-Hall, 1996.
[34] S. Tantaratana, "Polyphase structure with periodically time-varying coefficients: A realization for minimizing hardware subject to computational speed constraint," in *Proc. APCC*, Busan, Korea, Aug. 2006, pp. 1–5.
[35] R. Andraka and A. Berkun, "FPGAs make a radar signal processor on a chip a reality," in *Conf. Rec. 33rd Asilomar Conf. Signals, Syst., Comput.*, Pacific Grove, CA, USA, Oct. 24–27, 1999, vol. 1, pp. 559–563.
[36] R. G. Lyons, *Understanding Digital Signal Processing*, 2nd ed. Upper Saddle River, NJ, USA: Prentice-Hall, 2004.
[37] J. T. Johnson and L. C. Potter, "A study of detection algorithms for pulsed sinusoidal interference in microwave radiometry," *IEEE Trans. Geosci. Remote Sens.*, vol. 47, no. 2, pp. 628–636, Feb. 2009.
[38] B. Guner and J. T. Johnson, "Performance study of a cross-frequency detection algorithm for pulsed sinusoidal RFI in microwave radiometry," *IEEE Trans. Geosci. Remote Sens.*, vol. 48, no. 7, pp. 2899–2908, Jul. 2010.
[39] B. Guner, N. Niamsuwan, and J. T. Johnson, "Time and frequency blanking for RFI mitigation in microwave radiometry," *IEEE Trans. Geosci. Remote Sens.*, vol. 45, no. 11, pp. 3672–3679, Nov. 2007.
[40] R. D. DeRoo, S. Misra, and C. S. Ruf, "Sensitivity of the kurtosis statistic as a detector of pulsed sinusoidal RFI," *IEEE Trans. Geosci. Remote Sens.*, vol. 45, no. 7, pp. 1938–1946, Jul. 2007.
[41] J. R. Piepmeier, P. Mohammed, and J. Knuble, "A double detector for RFI mitigation in microwave radiometers," *IEEE Trans. Geosci. Remote Sens.*, vol. 46, no. 2, pp. 458–465, Feb. 2008.
[42] L. Li, P. Gaiser, M. R. Albert, D. G. Long, and E. M Twarog, "WindSat passive microwave polarimetric signatures of the greenland ice sheet," *IEEE Trans. Geosci. Remote Sens.*, vol. 46, no. 9, pp. 2622–2631, Sep. 2008.
[43] S. H. Yueh, "Estimates of Faraday rotation with passive microwave polarimetry for microwave remote sensing of Earth surfaces," *IEEE Trans. Geosci. Remote Sens.*, vol. 38, pt. 2, no. 5, pp. 2434–2438, Sep. 2000.
[44] N. Skou, S. S. Kristensen, T. Ruokokoski, and J. Lahtinen, "Onboard digital RFI and polarimetry processor for future spaceborne radiometer systems," in *Proc. IEEE IGARSS*, Munich, Germany, 2012, pp. 3423–3426.
[45] J. R. Piepmeier, E. Kim, P. Mohammed, J. Peng, and C. Ruf, "L1B_TB: Level 1B radiometer data product," Jet Propulsion Lab., Pasadena, CA, USA, 2012, *(SMAP: Algorithm Theoretical Basis Documents).* [Online]. Available: http://smap.jpl.nasa.gov/science/dataproducts/ATBD/
[46] M. W. Spencer, E. Njoku, D. Entekhabi, T. Doiron, J. Piepmeier, and R. Girard, "The HYDROS radiometer/radar instrument," in *Proc. IEEE IGARSS*, Anchorage, AK, USA, 2004, pp. 691–694.
[47] J. R. Piepmeier, "Radio Frequency Interference (RFI) in digital microwave radiometers," in *Proc. IEEE IGARSS*, Anchorage, AK, USA, 2004, pp. 1691–1694.

Jeffrey R. Piepmeier (S'93–M'99–SM'10) received the B.S. degree from LeTourneau University, Longview, TX, USA, in 1993 and the M.S. and Ph.D. degrees from Georgia Institute of Technology, Atlanta, GA, USA, in 1994 and 1999, respectively, all in electrical engineering.

He was with Vertex Communications Corporation and was a Schakleford Fellow with the Georgia Tech Research Institute, Atlanta. He is currently an Associate Head with the Microwave Instrument Technology Branch, NASA's Goddard Space Flight Center, Greenbelt, MD, USA. He is also a member of the Aquarius Science Team and an Instrument Scientist for the Soil Moisture Active Passive radiometer and the Global Precipitation Measurement Microwave Imager. His research interests include microwave radiometry and technology development for next-generation microwave sensors.

Dr. Piepmeier is a member of the International Union of Radio Science (URSI) Commission F and the American Geophysical Union. He was the Chair of the Instrumentation and Future Technologies Technical Subcommittee of the Geoscience and Remote Sensing Society and of the Committee on Radio Frequencies of the U.S. National Academies. He received an Excellence in Federal Career Gold Award (Rookie of the Year) in 2000 and was a 2002 NASA Earth Science New Investigator. He has received four NASA Group Achievement Awards and the NASA Exceptional Engineering Achievement Medal for advances in radio-frequency-interference mitigation technology and the NASA Exception Achievement Medal for significant contributions to the Aquarius/SAC-D mission.

Joel T. Johnson (S'88–M'96–SM'03–F'08) received the B.S. degree in electrical engineering from Georgia Institute of Technology, Atlanta, GA, USA, in 1991 and the S.M. and Ph.D. degrees from Massachusetts Institute of Technology, Cambridge, MA, USA, in 1993 and 1996, respectively.

He is currently a Professor with the Department of Electrical and Computer Engineering and The ElectroScience Laboratory, College of Engineering, The Ohio State University, Columbus, OH, USA. His research interests include microwave remote sensing, propagation, and electromagnetic wave theory.

Dr. Johnson is a member of the International Union of Radio Science (URSI) Commissions B and F, Tau Beta Pi, Eta Kappa Nu, and Phi Kappa Phi. He was named Office of Naval Research Young Investigator and was recognized by the U.S. National Committee of URSI as a Booker Fellow in 2002. He has served as an Associate Editor for the IEEE TRANSACTIONS ON GEOSCIENCE AND REMOTE SENSING since 2002. He received the Best Paper Award from the IEEE Geoscience and Remote Sensing Society in 1993, the National Science Foundation Career Award, and the Presidential Early Career Award for Scientists and Engineers in 1997.

Priscilla N. Mohammed (S'02–M'06) received the B.S. degree from Florida Institute of Technology, Melbourne, FL, USA, in 1999 and the M.S. and Ph.D. degrees from Georgia Institute of Technology, Atlanta, GA, USA, in 2001 and 2005, respectively, all in electrical engineering.

As a Ph.D. student, she performed microwave measurements of gaseous phosphine and ammonia under simulated conditions for the outer planets and used these measurements to develop a radio occultation simulator to predict absorption and excess Doppler due to Saturn's atmosphere. Much of this work was in support of the Cassini mission to Saturn. Based on these laboratory results, the Cassini Project Science Group made the decision to extend the Ka-band (32 GHz) operation throughout the mission tour. She is currently with Goddard Earth Sciences Technology and Research (GESTAR), Universities Space Research Association, Columbia, MD, USA, as a member of the Morgan State University research faculty and also with the Microwave Instrument Technology Branch, NASA's Goddard Space Flight Center, Greenbelt, MD. She is currently a member of the algorithm development team for the Soil Moisture Active Passive radiometer. Her research interests include radio-frequency-interference mitigation in microwave radiometers.

Damon Bradley (M'02) received the B.S. degree in electrical engineering from The Pennsylvania State University, White Oak, PA, USA, and the M.S. degree in electrical engineering from the University of Maryland, College Park, MD, USA. He is currently working toward the Ph.D. degree in electrical engineering with the University of Maryland, Baltimore, MD, studying the application of advanced signal processing methods for enabling passive microwave remote sensing of the Earth in the presence of interfering radio-frequency signals.

He is the Founder and the Leader of the Digital Signal Processing Technology Group, Instrument Electronics Development Branch, NASA's Goddard Space Flight Center, Greenbelt, MD. He is also the Radiometer Digital Electronics Subsystem DSP Team Leader on the NASA Soil Moisture Active Passive Radiometer.

Christopher Ruf (S'85–M'87–SM'92–F'01) received the B.A. degree in physics from Reed College, Portland, OR, USA, and the Ph.D. degree in electrical and computer engineering from the University of Massachusetts, Amherst, MA, USA.

He has previously worked with Intel Corporation, Hughes Space and Communications Company, the NASA Jet Propulsion Laboratory, and Pennsylvania State University, University Park, PA, USA. He is currently a Professor of atmospheric, oceanic, and space sciences; a Professor of electrical engineering and computer science; and the Director of the Space Physics Research Laboratory with the College of Engineering, University of Michigan, Ann Arbor, MI, USA. He is a Principal Investigator of the NASA Cyclone Global Navigation Satellite System Earth Venture mission. His research interests include GNSS-R bistatic scatterometry, microwave radiometry, atmosphere and ocean geophysical retrieval algorithm development, and sensor technology.

Dr. Ruf is a member of the American Geophysical Union (AGU), the American Meteorological Society (AMS), and the International Union of Radio Science Commission F. He has served as a member for the editorial boards of the IEEE TRANSACTIONS ON GEOSCIENCE AND REMOTE SENSING (IEEE TGRS), *AGU Radio Science*, and *AMS Journal of Atmospheric and Oceanic Technology*. He received four NASA Certificates of Recognition and seven NASA Group Achievement Awards, as well as the IEEE TGRS Best Paper Award in 1997, the IEEE Resnik Technical Field Award in 1999, and the Best Paper Award at the IEEE International Geoscience and Remote Sensing Symposium in 2006.

Mustafa Aksoy received the B.S. degree in electrical and electronic engineering from Bilkent University, Ankara, Turkey, in 2010. He is currently working toward the Ph.D. degree with The Ohio State University, Columbus, OH, USA.

He is currently a Graduate Research Associate with the ElectroScience Laboratory The Ohio State University. His research interests include microwave remote sensing and electromagnetic wave theory.

Rafael Garcia, photograph and biography not available at the time of publication.

Derek Hudson received the Ph.D. degree in electrical engineering from Brigham Young University, Provo, UT, USA, in 2009.

Since 2008, he has been with NASA's Goddard Space Flight Center, Greenbelt, MD, USA, working on calibration and system engineering for the radiometer on the Soil Moisture Active Passive mission.

Lynn Miles received the B.S. degree in electrical engineering from Morgan State University, Baltimore, MD, USA, in 2004 and the M.S. degree in electrical engineering from Johns Hopkins University, Baltimore, in 2010.

He is currently a member of the Digital Signal Processing Technology Group, Instrument Electronics Development Branch, NASA's Goddard Space Flight Center, Greenbelt, MD. He has been responsible for numerous tasks for various spaceflight and research projects, including the development of software development tools for data communications, data extraction, data analysis, calculation of higher order moments, and categorization of L-band radio-frequency interference.

Mark Wong received the B.S. degree from Georgia Institute of Technology, Atlanta, GA, USA, in 2002 and the M.S. and Ph.D. degrees from the University of Maryland, Baltimore, MD, USA in 2006 and 2010, respectively, all in electrical engineering.

Since 2009, he has been with NASA's Goddard Space Flight Center, Greenbelt, MD, where he is currently a Digital Signal and Image Processing Research Engineer working on high-speed imaging and computing spaceflight instruments.